

Near-surface composition and microhardness profile of plasma nitrided H-12 tool steel

E.J. Miola^a, S.D. de Souza^b, M. Olzon-Dionysio^b, D. Spinelli^a, M.R.F. Soares^c,
M.A.Z. Vasconcellos^d, C.A. dos Santos^{d,*}

^a Departamento de Materiais, EESC-USP, 13560-250 São Carlos SP, Brazil

^b Departamento de Física, UFSCar, 13565-950 São Carlos SP, Brazil

^c Instituto de Geociências, UFRGS, 91501-970 Porto Alegre RS, Brazil

^d Instituto de Física, UFRGS, C.P. 15051, 91501-970 Porto Alegre RS, Brazil

Received 23 March 1998; received in revised form 13 July 1998

Abstract

Samples of AISI H-12 tool steel were plasma nitrided at 500°C in a mixture of H₂–20% N₂ under a total pressure of 6 mbar, by using DC and pulsed glow discharges. The treatment time varied from 1 to 6 h. X-ray diffraction (glancing angle and θ – 2θ geometry), conversion electron Mössbauer spectroscopy, conversion X-ray Mössbauer spectroscopy, electron probe microanalysis, optical micrograph and Vickers microhardness were used as analytical techniques. The obtained results suggest that, under the present experimental conditions: (i) The near-surface compound layer consists of a mixture of γ' -Fe₄N and ϵ -Fe_x(N, C); (ii) the near-diffusion zone compound layer consists of a mixture of γ' -Fe₄N, ϵ -Fe_x(N, C), α'' -Fe₁₆N₂ and γ -austenite; (iii) the dependence of compound layer thickness on nitriding time violates the parabolic behavior and emphasizes effects from cathode sputtering and radiation-enhanced diffusion. © 1998 Elsevier Science S.A. All rights reserved.

Keywords: H-12 tool steel; Microhardness; Mössbauer spectroscopy; Plasma nitriding; X-ray diffraction

1. Introduction

The addition of nitrogen to steels, a process generically named nitriding, has been used for a long time in industry to improve the tribo-mechanical properties of engineering components [1–3]. Several techniques have been the subject of extensive studies: gas-nitriding, salt bath nitrocarburising, plasma nitriding (PN), ion implantation and plasma immersion ion implantation. In any case the tribo-mechanical properties of the treated materials are strongly related to the nature and size of the precipitates formed during the treatment, as well as their evolution when they are submitted to heating and, or, stresses during work. From X-ray diffraction analysis and metallography, it is known [4] that the near surface compound layer of PN steels consists mainly of ϵ carbonitrides and γ' -Fe₄N nitride. The ϵ carbonitride compounds comprise Fe₂(N, C), Fe_{3,2}(N, C) and

Fe_x(N, C), with $2 < x < 3.2$, hereafter ϵ_2 , ϵ_3 , and ϵ_x , respectively. Below this compound layer there is the so-called diffusion zone, α' , where the steel matrix is supersaturated by the in-diffusion nitrogen. Minor amounts of γ -austenite [5–8], dispersed alloy nitride precipitates [9], as well as cementite precipitates [10] have also been observed at the compound layer/diffusion zone interface of alloyed steels. As a whole, the compound plus diffusion zone thickness correlated very well with cross-section microhardness profile.

It is generally agreed that ionic bombardment plays two relevant roles on plasma nitriding [11]: first, it causes cathode sputtering and, second, it introduces point defects (mainly vacancies) at the near-surface region. Therefore, the compound layer growth in plasma nitriding is a complex diffusion process involving the well known parabolic law (settled by the so-called compound layer growth rate, CLGR), the sputtering rate (SR) and a competitive mechanism named radiation-enhanced diffusion (RED), where the usual thermal-induced jump rate of atoms are enhanced

* Corresponding author. Tel.: +55 51 3166424; fax: +55 51 3191762; e-mail: cas@if.ufrgs.br

due to defects created by ion irradiation [12]. It has been extensively investigated on the high energy (> 50 keV) ion implantation context [13]. Recent Monte Carlo modelling [14] demonstrated that RED leads to significant diffusion growth and to deep impurity penetration even for the case of low energy ion implantation. This is possible when low energy ion implantation is performed at high dose and high temperature, an operational condition bearing plasma nitriding.

Fig. 1 displays a schematic of ϵ and γ' layer growth by plasma nitriding, in light of cathode sputtering. Indeed, this picture is oversimplified because, as will be discussed below, CEMS and CXMS data imply that the compound layers are not single-phase. Poly-phase structure and detection of α' within the CEMS probed layer is presumably due to partial phase transformation after slow cooling down of the nitrided samples. For instance, γ' precipitates within ϵ and α' layers, and α' precipitates within γ' layer. In the same way, α'' -Fe₁₆N₂ and transformed austenite can be present near the diffusion zone.

Electron probe microanalysis (EPMA), X-ray diffraction (glancing angle, GXRD, or θ - 2θ geometry, XRD), conversion electron Mössbauer spectroscopy (CEMS) and conversion X-ray Mössbauer spectroscopy (CXMS) are complementary techniques very appropriate to investigate near-surface compound layer growth, in addition to microhardness profile. Typical thickness of compound layer in plasma nitrided steels is less than about 10 μm in samples treated during 2 h [2]. Since the depth probed by CEMS is about 0.2 μm in iron and steels, while that probed by CXMS is between 10 and 20 μm , it follows that changing from CEMS to CXMS it is possible to exhibit, qualitatively, the nitrided layer growth, in the same sense as the change from GXRD to XRD furnish qualitative depth profile for the near-sur-

face compound layer. Finally, careful cross-section EPMA measurements provide a direct view of the microstructure, as well as elemental profiles.

The literature is prodigious in works relating tribo-mechanical properties and nitriding parameters, but systematic studies related to the physical-chemical state of the nitrided steels are scarce. As a contribution to this subject we report a systematic study on a plasma nitrided AISI H-12 tool steel, by comparing the effect of DC and pulsed glow discharge on the physical-chemical state and kinetics of compound layer growth.

2. Experimental details

2.1. Sample preparation

After double tempering at 550°C, commercial samples of AISI H-12 tool steel (in wt%: 0.36 C, 0.87 Si, 0.43 Mn, 5.04 Cr, 1.73 Mo, 0.33 V, 1.14 W), were ground flat and mechanically polished to a 0.5 μm alumina finish. After that they were nitrided in an equipment similar to one described by Hudis [15]. A mixture of H₂-20% N₂ under a total pressure of 6 mbar was used for all samples. Voltage and current density were adjusted to maintain the cathode temperature at 500°C. The temperature was measured by a chromel–alumel thermocouple embedded in a control sample. Two operational modes were used: (i) conventional DC voltage applied between the workpiece and the wall of the furnace, hereafter DC glow discharge (DGD); (ii) pulsed voltage, operating at 9.83 kHz, referred to in the following as pulsed glow discharge (PGD). After nitriding during a time between 1 and 6 h the samples were submitted to a slow cooling down under vacuum, inside the treatment chamber.

2.2. Microhardness measurements

Cross-section microhardness profiles were performed in mirror polished surfaces etched with Nital 2%, following the method of measuring nitrided case depth for iron and steel described in the standard JIS G0562 [16]. All the measurements were done with a Zeiss microhardness tester equipped with a Vickers indenter, by using 0.07 kg load. Furthermore, conventional optical cross-section metallography was performed for all the samples.

2.3. X-ray diffractometry

X-ray diffraction patterns were performed in θ - 2θ geometry (XRD) and glancing angle geometry (GXRD) by means of a Siemens diffractometer D500, equipped with a curved graphite monochromator and CuK α

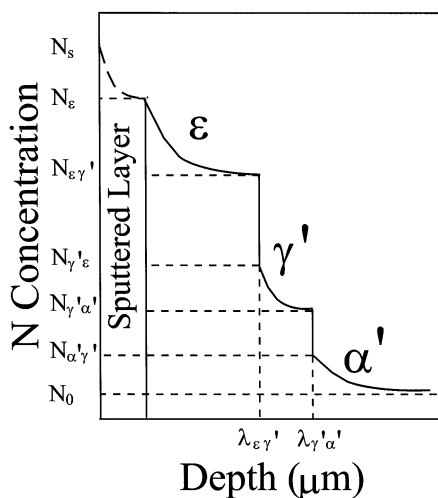


Fig. 1. Schematic illustration of ϵ and γ' layer growth, taking into account cathode sputtering. λ_{ij} is the interphase position.

radiation ($\lambda = 1.5418 \text{ \AA}$). XRD measurements were done with a scan step of $0.05^\circ 2\theta$ in the 2θ range from 10 to 80° , with a fixed counting time of 1 s , while GXRD patterns were obtained with fixed incidence angle at 3° , scan step of $0.02^\circ 2\theta$ and counting time of 4 s . For this incidence angle the thickness of the X-ray probed layer is about the same as that probed by the CEMS technique ($\cong 0.2 \text{ \mu m}$).

2.4. Electron probe microanalyses

EPMA measurements were performed with a CAMECA SX50 equipment using a 15 keV accelerating voltage, a 20 nA beam current, 1 \mu m probe diameter, and a takeoff angle of 40° . Intensities of $K\alpha$ line for carbon and nitrogen were recorded from steps of 1 \mu m during the scanning of the beam over the cross-section of the sample. These elements were analysed with synthetic multilayer crystal ($2d = 9.68 \text{ nm}$). Each reported profile is an average over five measurements, taken at corresponding points along several longitudinal directions.

2.5. Mössbauer spectroscopy

The Mössbauer spectroscopy data were obtained in a backscattering geometry. A proportional counter in which $\text{He}-5\% \text{ CH}_4$ (for CEMS) or $\text{Ar}-5\% \text{ CH}_4$ (for CXMS) was allowed to flow, was added to a conventional constant acceleration Mössbauer spectrometer. The source was ^{57}Co in a Rh matrix with a nominal activity of 25 mCi . All the CEMS and CXMS measurements were performed at room temperature (RT). Isomer shifts are given relative to $\alpha\text{-Fe}$ at RT.

3. Results

3.1. Crystallographic and chemical state of the compound layer

Fig. 2 shows XRD patterns for the samples nitrided at 1 , 4 and 6 h , using the DGD process. There is no evidence of the steel matrix reflections (essentially a martensite structure), even for the smallest nitriding time. Therefore, we concluded that the effective compound layer thickness is larger than the effective range probed by the $\text{CuK}\alpha$ radiation [17], roughly 10 \mu m . The compound layer comprises essentially $\epsilon\text{-Fe}_{2-3}(\text{C},\text{N})$ and $\gamma'\text{-Fe}_4\text{N}$. The ϵ carbonitride layer is highly textured along the $\langle 101 \rangle$ direction for the sample nitrided at 1 h , but shows a clear polycrystalline character for increasing nitriding time. The γ' reflections are virtually absent from the XRD pattern for the sample nitrided at 1 h and growth monotonically with the increasing of the nitriding time. This behavior is somewhat different for

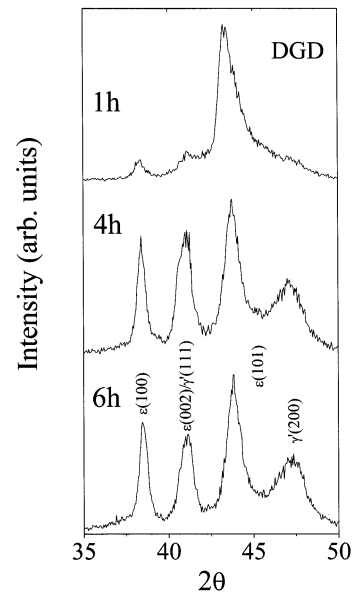


Fig. 2. $\theta-2\theta$ X-ray diffractograms for DGD samples nitrided during 1 , 4 and 6 h . The indexed reflections are indicated.

the PGD samples. As can be seen in Fig. 3, the normalised intensity of the $\epsilon\{100\}$ reflection for the sample nitrided at 1 h is about 70% of that measured for the sample nitrided at 6 h . Therefore, at the initial step of the nitriding process the contribution from the γ' component is more significant for PGD samples than for DGD ones. The patterns displayed in Figs. 2 and 3 suggest that the situation is reversed after 4 h . This trend can be best appreciated by GXRD measurements, as clearly shown in Fig. 4 for the samples nitrided during 6 h . The $\gamma'\{200\}$ normalised intensity is 0.17 for the PGD sample and 0.29 for the DGD one.

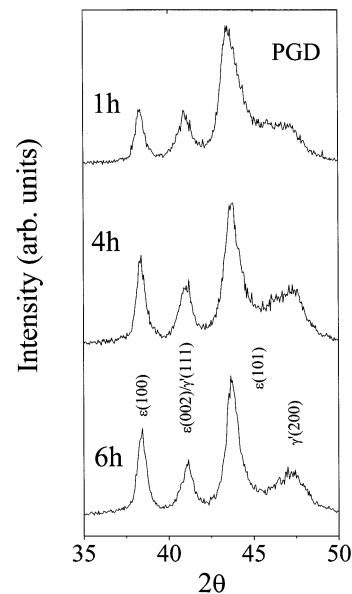


Fig. 3. $\theta-2\theta$ X-ray diffractograms for PGD samples nitrided during 1 , 4 and 6 h . The indexed reflections are indicated.

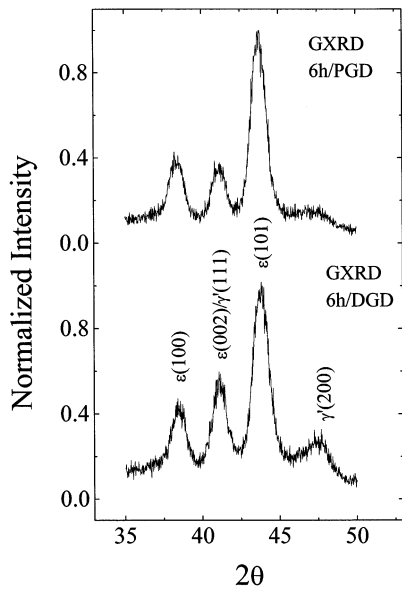


Fig. 4. Glancing-angle X-ray diffractograms for PGD and DGD samples nitrided during 6 h. The indexed reflections are indicated.

The CEMS spectrum for the as-received sample confirms the XRD measurements as the hyperfine parameters can be attributed to α' -(Fe,C,N) martensite [18]. Fig. 5 displays CEMS spectra for PGD samples whose XRD patterns are shown in Fig. 3. These spectra

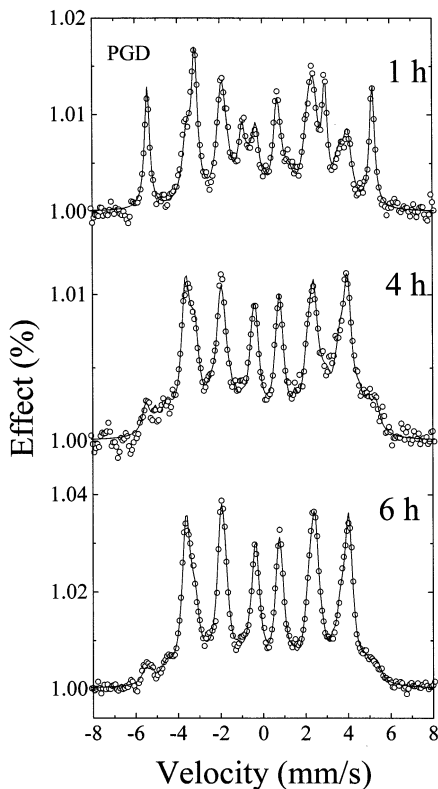


Fig. 5. CEMS spectra for PGD samples nitrided during 1, 4 and 6 h. The continuous curves represent fitted spectra, as illustrated in Fig. 6.

Table 1

Typical values of the parameters used to fit the different ^{57}Fe CEMS and CXMS spectra shown in this work

Component	H (kG)	ΔE_Q (mm s $^{-1}$)	δ (mm s $^{-1}$)
α' -martensite	331	0.01	0.01
γ -(Fe-N-C) austenite	—	—	-0.12
		0.32	0.05
α'' -Fe $_{16}$ N $_2$	314	0.09	0.17
ε -Fe $_{3.2}$ (C, N)	290	0.02	0.29
	241	0.02	0.32
ε -Fe $_{2+x}$ (C, N)	220	0.03	0.32
$x < 1.2$	108	0.01	0.51
	—	0.95	0.45
γ' -Fe $_4$ N	338	0.02	0.25
	210	0.25	0.32

The isomer shifts are given relative to α -Fe. Typical errors are: $\pm 3\%$.

were fitted by the addition of sub-spectra corresponding to α' , γ' , ε_3 and ε_x , with typical hyperfine parameters as displayed in Table 1, which are quite similar to those previously published [19–23]. ε_3 represents the carbonitride ε -Fe $_{3.2}$ (C, N), while ε_x stands for ε -Fe $_x$ (C, N), with $2 \leq x < 3.2$. A typical fitting, showing the subspectra, is illustrated in Fig. 6 for the DGD sample nitrided during 1 h. This spectrum was fitted to 30% of α' , 30% of γ' , 33% of ε_3 and 7% of ε_x . The CEMS spectrum for the PGD sample nitrided during 1 h (see Fig. 5) consists of 31% of α' , 20% of γ' , 33% of ε_3 and 16% of ε_x . For nitriding time $t \geq 2$ h, all the CEMS spectra are quite similar for both processes. Minor differences, as reflected by the relative spectral areas, can only be discriminated by the fitting procedures. These trends

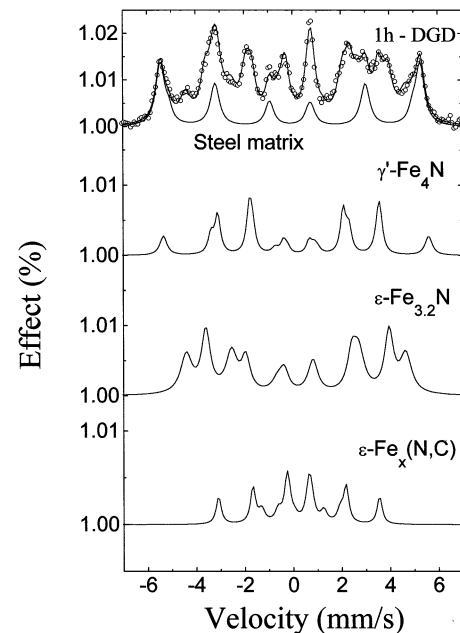


Fig. 6. CEMS spectrum for DGD sample nitrided during 1 h, showing the subspectra used in the fitting procedure.

Table 2

Relative CEMS and CXMS spectral areas for samples nitrided at DC glow discharge (DGD) condition

Nitriding time (h)	α' CEMS/CXMS	α'' CEMS/CXMS	γ CEMS/CXMS	γ' CEMS/CXMS	$\varepsilon_{3,2}$ CEMS/CXMS	ε_x ($x < 3.2$) CEMS/CXMS
1	30/49	0/13	0/5	30/4	33/19	8/10
2	14/—	0/—	0/—	23/—	54/—	9/—
3	12/42	0/6	0/0	25/12	54/34	9/7
4	12/39	0/5	0/2	25/10	53/37	10/7
5	—/42	—/8	—/3	—/13	—/29	—/5
6	7/—	0/—	0/—	35/—	51/—	7/—

Typical errors are $\pm 5\%$

are also observed for the CXMS measurements, as can be seen in Table 2 and Table 3. As an illustration, Fig. 7 displays the CXMS result obtained for the PGD sample nitrided at 1 h. General outlook of the compound layer evolution is illustrated by plotting the relative spectral areas (see Table 2) as a function of the nitriding time. Fig. 8 (PGD samples) and Fig. 9 (DGD samples) are consistent with the XRD measurements in what concerns the compound layer growth. For instance, the relative spectral area attributed to $\varepsilon_{3,2} + \varepsilon_x$ (referred to as ε in the Figs. 8 and 9) account for 49% of the total spectrum for the PGD sample and 40% for the DGD one, in close accord to Figs. 2 and 3. In addition, the DGD sample shows a remarkable increasing of the γ' component (see Fig. 9) for nitriding time $t > 3$ h, confirming the results displayed in Fig. 4.

The carbon present in the steel matrix, in addition to its increased concentration due to treatment contamination, could induce θ -Fe₃C precipitation. We have tried to use the parameters from this phase [24] in our fitting scheme to the CXMS spectra, but they were unequivocally ruled out. As expected, α'' -Fe₁₆N₂ precipitation was observed on the CXMS spectra as a consequence of the slow cooling down. In the discussion above, the small spectral area attributed to α'' -Fe₁₆N₂ was not considered. CXMS measurements have also suggested the existence of minor amounts of γ -austenite near the diffusion zone. The quadrupolar doublet present at the CXMS spectra have been observed in iron submitted to successive implantation of nitrogen and carbon, but was not attributed to any known nitride or carbide [25]. We propose now this doublet and the singlet with $\delta_{Fe} = -0.12$ mm s⁻¹ to be attributed to γ austenite containing carbon and nitrogen. Under equilibrium conditions, the formation of an austenitic phase is not possible below 840 K. However, plasma nitriding, like ion implantation, is a non-equilibrium treatment. In a previous work Kurny et al. [26] explained the formation of austenite during ion nitriding of armco iron by considering the possibility of nitrogen diffusion from the supersaturated γ' phase to the α matrix, which becomes very rich in nitrogen and eventually transforms in austenite. It is interesting to note that the

experimental conditions used by those authors are very similar to those used in the present work. Fe–N austenite has been also observed in 38NCD4 steel [27] and iron [28] implanted with nitrogen.

In addition to the above proposal from Kurny et al. [26], a plausible mechanism can be associated to localised heating induced by the high energy ion bombardment, raising the local temperature to above the average value as measured by the thermocouple. This mechanism has been ascribed to the formation of austenite on the N-implanted materials [27]. Perhaps an additional effect is present. The carbon-rich region near the diffusion zone (see discussion below) can behave locally as a high-carbon steel. Thus, after the formation of austenite by one or another mechanism describe above, it can be retained at room temperature because of the large amount of carbon. Unfortunately austenite is observable in such small amount that it is below the XRD detection limit. We are able to detect it by Mössbauer measurements because this component is paramagnetic, with subspectrum composed of a doublet and a singlet, which can easily be distinguished from the magnetic sextets of the other components.

3.2. Cross-section profiles

Three kinds of cross-section profiles were measured: optical micrograph, Vickers microhardness and semi-quantitative EPMA nitrogen concentration. In Fig. 10 an optical micrograph is illustrated for DGD sample nitrided during 5 h. Typical Vickers microhardness profiles as a function of depth from the nitrided surface are depicted in Fig. 11 for DGD samples nitrided during 3 and 4 h. Semi-quantitative nitrogen cross-section profiles are shown in Fig. 12 for DGD and PGD samples nitrided during 3 and 4 h.

Within experimental and methodological limitations, all these techniques furnish similar depth-profiles. Compound layer thickness can be estimated from Fig. 10 by visual evaluation. On the other hand, thickness of the hard cases can be estimated from the microhardness profiles by arbitrarily assuming 800 HV as the minimum hardness of the nitrided layer (the hardness of

Table 3

Relative CEMS and CXMS spectral areas for samples nitrified at pulsed glow discharge (PGD) condition

Nitriding time (h)	α' CEMS/ CXMS	α'' CEMS/ CXMS	γ CEMS/ CXMS	γ' CEMS/ CXMS	$\epsilon_{3,2}$ CEMS/ CXMS	ϵ_x ($x < 3.2$) CEMS/ CXMS
1	31/48	0/10	0/4	20/7	33/26	16/5
2	10/—	0/—	0/—	19/—	64/—	7/—
3	7/40	0/9	0/2	21/7	66/35	6/7
4	11/—	0/—	0/—	25/—	54/—	10/—
5	—/40	—/10	—/2	—/11	—/33	—/4
6	5/—	0/—	0/—	24/—	61/—	11/—

Typical errors are $\pm 5\%$

tempered H-12 steel, before nitrifying, is 600 ± 50 HV). As illustrated in Fig. 11, the hard case thickness is about $45 \mu\text{m}$ for DGD sample nitrified during 3 h and about $85 \mu\text{m}$ for that nitrified during 4 h. The compound layer and hard case thicknesses as a function of the nitriding time are plotted in Fig. 13 for all DGD and PGD samples. The similarities between the curves are remarkable. For nitriding time $t \leq 3$ h the PGD compound layer thickness (hard case) is thicker than the DGD one, while the inverse is true for nitriding time $t > 3$ h. This behavior is supported by EPMA measurements. As can be seen Fig. 12, the profile thickness for DGD sample nitrified at 4 h is remarkably larger than that for PGD sample, while, within the experimental error, they are equal for nitriding time $t = 3$ h.

Carbon profile measurements were performed, but the large scatter of the data disallow us to establish a conclusive interpretation. The inset shown in Fig. 12 is one of the most regular carbon profile. As will be discussed below, other authors [2,29–31] have reported this kind of profile. In spite of the scatter and the fail to reproduce the same pattern, all the carbon profiles show a net trend as illustrated in Fig. 12. That is to say a near-surface decarburized region and a carbon-rich region near the compound layer/steel matrix interface.

The hard case thickness as a function of the square root of the nitriding time, shown in Fig. 14, represent the kinetics of the compound layer growth for DGD

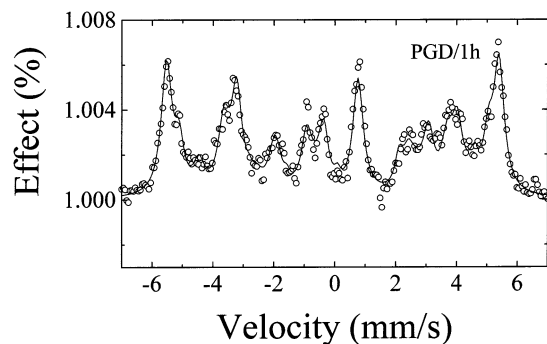


Fig. 7. CXMS spectrum for PGD sample nitrified at 1 h. The continuous curves represent fitted spectra, as illustrated in Fig. 6.

and PGD samples. The DGD curve, Fig. 14(a), obeys the parabolic law, although a tendency for saturation is suggested for nitriding time $t > 5$ h. The PGD curve, Fig. 14(b), clearly deviates from the parabolic law. It appears the compound layer for PGD samples growth at steps with different kinetics. At the initial stage ($t < 3$ h) the compound layer thickness grows faster than at the final stage ($t > 2$ h). As we shall discuss, similar results have been reported for several materials plasma nitrified at different process parameters [7,32–35].

4. Discussion

4.1. Crystal and chemical state of the compound layer

Mössbauer spectroscopy and X-ray diffraction measurements are entirely consistent as concerned to the chemical composition of the near-surface nitrified layer. However, some particular details are discriminated by each one of these techniques. For instance, the textured growth of the ϵ carbonitride layer is clearly indicated by XRD for the sample nitrified during 1 h with a DC glow discharge, while for the pulsed glow discharge a polycrystalline layer, comprising randomly oriented crystallites, is strongly suggested (see Figs. 2 and 3). Samples prepared in different batches have systemati-

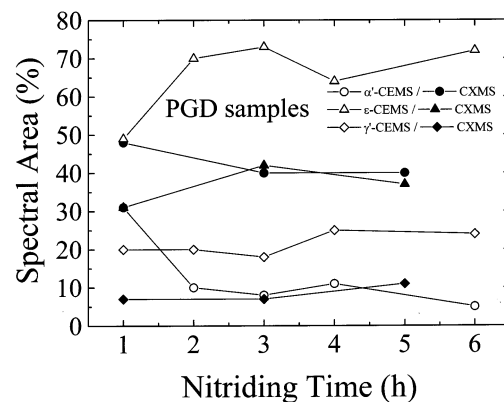


Fig. 8. Relative spectral areas for CEMS (open symbols) and CXMS (solid symbols) spectra from PGD samples.

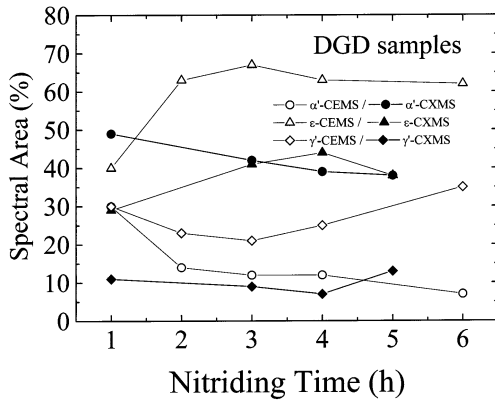


Fig. 9. Relative spectral areas for CEMS (open symbols) and CXMS (solid symbols) spectra from DGD samples.

cally shown this kind of behavior, which appears to be a process-dependent phenomenon. A possible explanation could be the continuous surface bombardment by energetic ions, which take place when DC plasma is used, as compared to the interrupted one when the pulsed plasma is used. Thus, the outer ϵ carbonitride layer is continuously sputtered during the DGD process and for small processing times (≤ 1 h) it remains thin, which would favour the retention of the $\langle 101 \rangle$ texture. For larger times the ϵ carbonitride layer is thick enough and the texture is destroyed. On the contrary, for a PGD process ionic bombardment is essentially limited to the power-on cycle. Meanwhile nitriding is sustained by the active species [36] and the outer compound layer increases, destroying the $\langle 101 \rangle$ texture even for the smallest nitriding time.

CEMS and CXMS also emphasise some details not suggested by XRD measurements. For instance, based on XRD data it is not possible to discriminate ϵ - $\text{Fe}_x(\text{C}, \text{N})$ precipitates with different stoichiometry. However, as these metastable carbonitrides have different hyperfine parameters, mostly different hyperfine field, it becomes quite feasible to discriminate them by

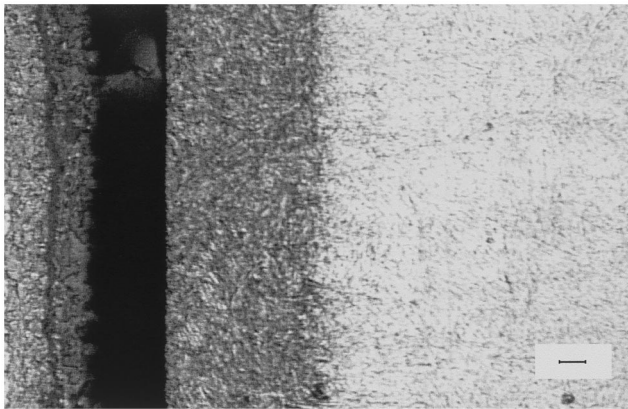


Fig. 10. Cross-section optical micrograph for DGD sample nitrided during 5 h.

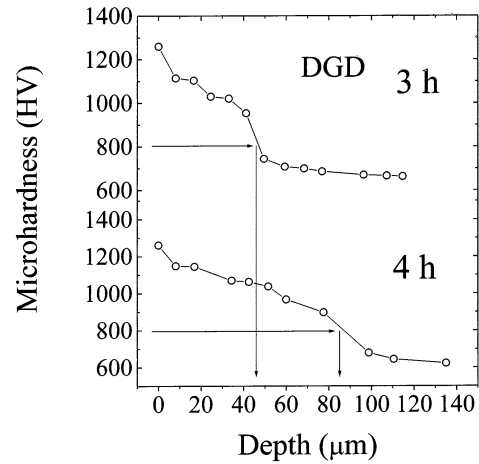


Fig. 11. Vickers microhardness profiles as a function of depth from the nitrided surface for DGD samples nitrided during 3 and 4 h.

fitting CEMS and CXMS spectra, as illustrated in Fig. 6. Nevertheless, the main purpose here is not to distinguish between different ϵ carbonitrides, but to compare the dependence of ϵ (i.e. $\epsilon_x + \epsilon_{3,2}$) and γ' relative spectral areas on the nitriding condition (DGD vs PGD). Table 2; Figs. 8 and 9 summarize data on these subject.

As shown in Figs. 8 and 9, the CEMS ϵ/γ' spectral area ratio for the sample nitrided at $t = 1$ h is about 2.5 for the PGD sample and about 1.3 for the DGD one. Therefore, the ϵ layer in PGD sample is very thicker than that in DGD one, supporting the argument used above in discussing the $\langle 101 \rangle$ texture observed on the XRD measurement. In comparing the effect of DGD and PGD processes on the compound layer growth kinetics, it is interesting to observe the evolution of the γ' layer. The γ' spectral area is almost constant (between 20 and 25% for CEMS spectra and between 8

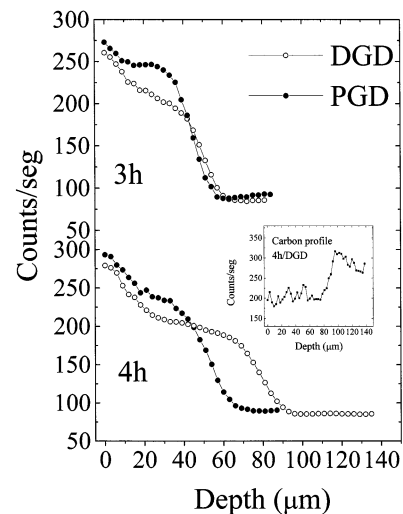


Fig. 12. Semi-quantitative nitrogen cross-section profiles are shown for DGD and PGD samples nitrided during 3 and 4 h. The inset shows the carbon profile for DGD sample nitrided during 4 h.

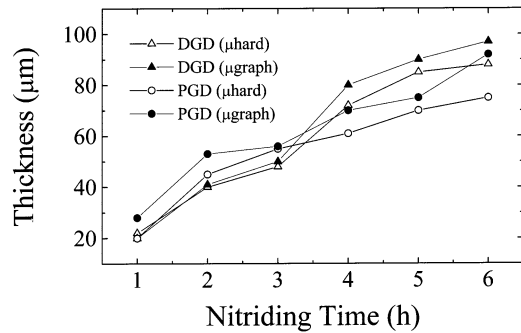


Fig. 13. Compound layer (μ graph) and hard case (μ hard) thickness as a function of the nitriding time for DGD and PGD samples.

and 10% for CXMS) for all PGD samples, while it changes considerably as function of the nitriding time for DGD samples. Particularly interesting is the γ' increasing tendency and the α' decreasing displayed in Fig. 9 for CXMS spectra. This behavior suggests that the DGD compound layer ($\varepsilon + \gamma'$) is thicker than the PGD one for nitriding time $t > 4$ h, in complete agreement with Fig. 13.

4.2. Nitrogen and carbon cross-section profile

As expected, nitrogen profiles, as measured by EPMA, are entirely consistent with cross-section profiles obtained from optical micrograph and microhardness measurements (see Figs. 10–13). Differently,

carbon profile measurements have been quite disperse, although a curious trend is clearly exhibited for all the samples. We are referring to the carbon-rich region observed near the compound layer/steel matrix interface, as illustrated in Fig. 12. In addition to carbon pre-existent in the steel matrix, residual carbonaceous gas molecules in the vacuum chamber during sample preparation and EPMA measurements, as well as carbon remaining after the mechanical polishing treatment are the major factors controlling the near-surface carbon contamination. Such carbon contamination has been described, for instance, during implantation of Ti ions at high fluences [37]. Therefore, while nitrogen profiles for equivalent samples from different batches are almost the same, the carbon profiles appear to be strongly dependent on some uncontrolled preparation conditions.

Once at the near-surface layer, carbon atoms spread out according to the model proposed by Sun and Bell [2] to explain the recurrent observation of decarburized zones near the surface and carbon-rich zones in the nitriding front of plasma nitrided low alloy steels. According to this model the compressive stresses and the uptake of nitrogen in the nitrided layer cause carbon redistribution: the carbon atoms in the steel will diffuse to stress-free region, i.e. towards the surface and the diffusion zone.

4.3. Kinetic behavior

The results displayed in Fig. 14 can be explained as following. At the beginning of the plasma nitriding process (DGD or PGD) SR is expected to be more important than RED, because the defect layer is in the main inside the sputtered layer. Because of continuous ionic bombardment, SR and RED are more significant in DGD than in PGD. Therefore, the outer surface of the DGD sample is sputtered more extensively than that of the PGD sample. For this reason the PGD compound layer is thicker than the DGD one for $t < 3$ h.

As the nitriding time increases to moderate values RED becomes more important, because the defect layer diffuses away, escaping from the sputtering effect. In such condition, the DGD compounds layer grows faster than the PGD one. With further nitriding time increasing, to t_{sat} , SR and RED effects become equivalent [14] and global saturation is attained. Fig. 14 suggests $t_{\text{sat}} \geq 6$ h for DGD and $t_{\text{sat}} > 6$ h for PGD. From simulation of formation of iron nitrides during plasma nitriding of α -Fe it was obtained $t_{\text{sat}} \cong 4$ h [34]. Considering the substrate effect on compound layer growth, the simulation fits very well our experimental results. The saturation time from Fig. 14 is also quite similar to that published for the same steel used in the present work [32].

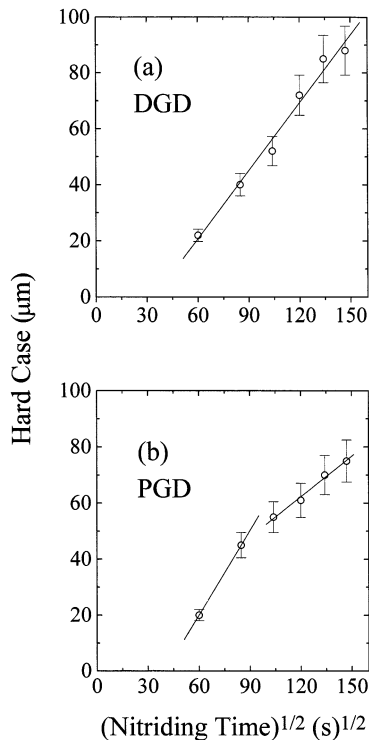


Fig. 14. Hard case thickness as a function of square root of the nitriding time for (a) DGD and (b) PGD samples.

The transition from high-rate regime to a lower one corresponds to the moment at which SR becomes meaningful for PGD samples. It seems that the absence of the high-rate regime in DGD process is due to the continuous ionic bombardment, with no power-off interval.

5. Conclusions

A systematic investigation of crystal and chemical state of compound layer and cross-section microhardness profile was undertaken on AISI H-12 tool steel treated by DC glow discharge (DGD) and by pulsed glow discharge (PGD). X-ray diffraction (XRD), conversion electron Mössbauer spectroscopy (CEMS), conversion X-ray Mössbauer spectroscopy (CXMS), electron probe microanalysis (EPMA), optical micrograph and Vickers microhardness were used as analytical techniques. The results suggest that, under the present experimental conditions:

(i) The near-surface compound layer, as probed by CEMS, consists of a mixture of γ' -Fe₄N and ε -Fe_x(N, C).

(ii) The near-diffusion zone compound layer, as probed by CXMS, consists of a mixture of γ' -Fe₄N, ε -Fe_x(N, C), α'' -Fe₁₆N₂ and γ -austenite. Three mechanisms can be accountable for the formation of austenite in the present samples: (a) nitrogen relieves from the supersaturated γ' phase to the α' matrix, which becomes very rich in nitrogen and eventually transforms in austenite; (b) localised heating induced by the high energy ion bombardment, raising the local temperature to above the average value as measured by the thermocouple; (c) the carbon-rich region near the diffusion zone can behave locally as a high-carbon steel. Thus, after the formation of austenite by (a) or (b), it can be retained at room temperature because of the large amount of carbon.

(iii) Cross-section profiles, from optical micrograph and EPMA are consistent with that from Vickers Microhardness.

(iv) The kinetic behavior violates the parabolic law and emphasis effects from cathode sputtering and radiation-enhanced diffusion (RED). Consistently with sputtering effects and RED, for nitriding time $t < 2$ h, the PGD compound layer is thicker than DGD one. The situation is reversed for $t > 3$ h.

Acknowledgements

We are much indebted to Dr F.C. Zawislak and Dr P.M Mors for stimulating discussions. One of us (EM) acknowledges the hospitality of the IF-UFRGS staff during his stay at Porto Alegre. This work has been

partly supported by the Brazilian agencies CAPES, CNPq, FINEP and FAPERGS.

References

- [1] J.R. Conrad, J.L. Radtke, R.A. Dodd, R.J. Worzala, N.C. Tran, *J. Appl. Phys.* 62 (1987) 4591.
- [2] Y. Sun, T. Bell, *Mater. Sci. Eng. A* 140 (1991) 419.
- [3] G.A. Collins, R. Hutchings, J. Tendys, M. Samandi, *Surf. Coat. Technol.* 68 (1994) 285.
- [4] B. Edenhofer, *Heat Treat. Metals*, 1 (1974) 23; 1(1974) 59.
- [5] G.A. Collins, R. Hutchings, J. Tendys, M. Samandi, *Surf. Coat. Technol.* 68 (1994) 285.
- [6] Z. Nitkiewicz, L. Jeziorski, *Mater. Sci. Eng. A140* (1991) 469.
- [7] U. Figueroa, J. Oseguera, P.S. Schabes-Retchkiman, *Surf. Coat. Technol.* 86 (1996) 728.
- [8] G. Simon, M.A.Z. Vasconcellos, C.A. dos Santos, In: *Proc. Int. Conf. on the Applications of the Mössbauer Effect*, Rimini, Italy, 1995, p. 185.
- [9] P.C. van Wigen, H.C.F. Rozendaal, E.J. Mittemeijer, *J. Mater. Sci.* 20 (1985) 4561.
- [10] E. Haruman, T. Bell, Y. Sun, *Surf. Eng.* 8 (1992) 275.
- [11] E.I. Meletis, S. Yan, *J. Vac. Sci. Technol.* A11 (1993) 25.
- [12] G.L. Dienes, D.C. Damask, *J. Appl. Phys.* 29 (1958) 1713.
- [13] E. Antoncik, *Radiat. Eff.* 116 (1991) 375; 127 (1993) 75.
- [14] S.H. Valiev, T.S. Pugacheva, F.G. Jurabekova, S.A. Lem, Y. Miyagawa, *Nucl. Instrum. Meth. Phys. Res. B* 127 (1997) 265.
- [15] M. Hudis, *J. Appl. Phys.* 44 (1973) 1489.
- [16] JIS G0562 Standard, *Surf. Eng.* 11 (1995) 57.
- [17] R. Delhez, T.H. de Keijser, E.J. Mittemeijer, *Surf. Eng.* 3 (1987) 331.
- [18] N. DeCristofaro, R. Kaplow, *Metall. Trans.* A8 (1977) 35.
- [19] K.H. Eickel, W. Pitsch, *Phys. Status Solidi.* 39 (1970) 121.
- [20] A.J. Nozik, J.C. Wood, G. Haacke, *Solid State Commun.* 8 (1970) 8.
- [21] G. Le Caer, A. Simon, A. Lorenzo, J.M. Génin, *Phys. Status Solidi A* 6 (1971) 97.
- [22] D. Firrao, M. Rosso, G. Principi, R. Frattini, *J. Mater. Sci.* 17 (1982) 1773.
- [23] C.A. dos Santos, B.A.S. de Barros, J.P. de Souza, I.J.R. Baumvol, *Appl. Phys. Lett.* 41 (1982) 237.
- [24] M. Ron, Z. Mathalone, *Phys. Rev. B* 4 (1971) 774.
- [25] C.A. dos Santos, I.J.R. Baumvol, E.A. Garcia, M. Behar, *J. Phys. D: Appl. Phys.* 17 (1984) 969.
- [26] A.S. Kurny, R.M. Mallya, M. Mohan Rao, *J. Less Common. Metals* 144 (1988) 201.
- [27] M. Carbucicchio, L. Bardani, S. Tosto, *J. Appl. Phys.* 52 (1981) 4589.
- [28] B. Rauschenbach, A. Kolitsch, *Phys. Stat. Sol.* 80 (1983) 211.
- [29] M.A.J. Somers, E.J. Mittemeijer, *Surf. Eng.* 3 (1987) 123.
- [30] M.A.J. Somers, P.F. Colijn, W.G. Sloof, E.J. Mittemeijer, *Z. Metallkde.* 81 (1990) 33.
- [31] M. Samandi, A. Pauza, G. Hatziandoniou, H. Yasbandha, R. Hutchings, G.A. Collins, J. Tendys, *Surf. Coat. Technol.* 54 (1992) 447.
- [32] J.L. Albarran, J.A. Juárez-Islas, L. Martinez, *Mater. Lett.* 15 (1992) 68.
- [33] J. D'Haen, C. Quasyhaegens, G. Knuyt, M. D'Olieslaeger, L.M. Stals, *Surf. Coat. Technol.* 74 (1995) 405.
- [34] V.I. Dimitrov, J. D'Haen, G. Knuyt, C. Quasyhaegens, L.M. Stals, *Appl. Phys. A63* (1996) 475.
- [35] Y. Sun, T. Bell, *Mater. Sci. Eng.* A224 (1997) 33.
- [36] H. Michel, T. Czerwec, M. Gantois, D. Ablitzer, A. Ricard, *Surf. Coat. Technol.* 72 (1995) 103.
- [37] I.L. Singer, *J. Vac. Sci. Technol.* A1 (1983) 419.